Materials Today Chemistry 22 (2021) 100570

Contents lists available at ScienceDirect

Materials Today Chemistry

journal homepage: www.journals.elsevier.com/materials-today-chemistry/

Water-annealing regulated protein-based magnetic nanofiber materials: tuning silk structure and properties to enhance cell response under magnetic fields

Y. Xue [a, b, c], K. Jackson [b], N. Page [a], X. Mou [d], S. Lofland [a], X. Hu [a, b, e, *]

[a] Department of Physics and Astronomy, Rowan University, Glassboro, NJ 08028, USA
[b] Department of Biomedical Engineering, Rowan University, Glassboro, NJ 08028, USA
[c] School of Life Sciences, Nantong University, Nantong, 226019, China
[d] Department of Chemistry and Biochemistry, Rowan University, Glassboro, NJ 08028, USA
[e] Department of Molecular and Cellular Biosciences, Rowan University, Glassboro, NJ 08028, USA

ARTICLE INFO

Article history:
Received 15 June 2021
Received in revised form
18 August 2021
Accepted 24 August 2021
Available online xxx

Keywords:
Silk fibroin
Barium ferrite
Electrospun fibers
Hybrid magnetic biomaterial
Water annealing

ABSTRACT

In this study, flexible silk fibroin protein and biocompatible barium hexaferrite (BaM) nanoparticles were combined and electrospun into nanofibers, and their physical properties could be tuned through the mixing ratios and a water annealing process. Structural analysis indicates that the protein structure of the materials is fully controllable by the annealing process. The mechanical properties of the electrospun composites can be significantly improved by annealing, while the magnetic properties of barium hexaferrite are maintained in the composite. Notably, in the absence of a magnetic field, cell growth increased slightly with increasing BaM content. Application of an external magnetic field during *in vitro* cell biocompatibility study of the materials demonstrated significantly larger cell growth. We propose a mechanism to explain the effects of water annealing and magnetic field on cell growth. This study indicates that these composite electrospun fibers may be widely used in the biomedical field for controllable cell response through applying different external magnetic fields.

1. Introduction

Magnetic materials are beginning to play a significant role in the biomedical field. Through the use of an external magnetic field, magnetic nanoparticles (MNPs) can be influenced to perform tasks such as delivering drugs to specific sites of the body [1–3] or increasing the temperature in a specific region of the body to eliminate malignant cells [4–6]. Attaching biological labels such as antibodies to MNPs allows them to detect various biomolecules so they can be used in biosensors and the diagnosis of certain ailments [7,8].

Incorporating magnetic nanoparticles into biocompatible polymers provides a means for protecting the magnetic material from its surrounding environment, as well as shielding a living organism from the potential toxicity of the compound [9]. In tissue engineering, cells can be magnetically labeled so that a magnet can guide the cells to form desired two-dimensional and three-dimensional structures to later differentiate and form desired tissues. A magnetic polymer scaffold could be used as a more localized and noninvasive means of using the many applications of MNPs *in vitro* and *in vivo* [10]. Primarily, magnetic scaffolds could enhance tissue engineering by directing magnetically labeled cells, growth factors, and other needed material in a way that contributes to tissue development both before and after implantation into the body [11]. The use of an external magnetic field to cause physical changes in the magnetic scaffolds, like stretching or contracting [12,13], could provide mechanical cues to cells that could also help tissue development [14]. Additionally, drugs labeled with MNPs could be led by the scaffold to specific regions of the body, or an external magnetic field could cause the scaffold to release drugs as needed by the body [14–16].

Common magnetic materials include magnetite, hematite, and barium hexaferrite [17–20]. These magnetic materials have been used in mobile communication, information technology, and biomedical engineering [21–26], but cells are very sensitive to the scaffold environment. Therefore, it is critical to choose the

---

* Corresponding author.
E-mail address: hu@rowan.edu (X. Hu).

https://doi.org/10.1016/j.mtchem.2021.100570
2468-5194/

appropriate magnetic material to be incorporated into the composite scaffold according to its magnetic permeability, magnetization, electrical resistivity, and the interactions between the material and the matrix. Due to its good biocompatibility, low cytotoxicity, and high magnetic permeability, ferrites are the most promising magnetic materials for biomedical applications [27,28].

Silk is one of the proteins commonly used as a natural polymer to make protein-based biomaterials [29–32]. Silk fibers mainly consist of the protein fibroin, which appears as a double-stranded fiber, and sericin, which coats the fibroin fibers and bonds them together. Silk fibroins can be easily fabricated into various structures such as films, fibers, gels, particles, and scaffolds [29,33–37]. Due to its predominant β-sheet crystal structure, silk fibroins are also known to have excellent mechanical stability and tunability in terms of its biodegradation rates and mechanical properties [38–41]. The physical and chemical properties of silk fibroins can vary based on different amino acid sequences, artificial treatments with substances such as methanol, and composites resulting from mixing silk with various functional materials [29,42]. Recently, a water annealing method was found to induce up to 30% crystallization of beta sheets [43,44]. That crystalline structure in the silk protein matrix can act as a crosslinker to efficiently encapsulate small inclusions such as nanoparticles or inorganic drugs in the matrix [43,44].

Although magnetic nanoparticles have many potential applications in tissue engineering, nanoparticles alone cannot mimic the extracellular matrix to promote cell growth. Studies have shown that nanofibers prepared by electrospinning can be used to prepare tissue scaffolds [45–47]. Because the tissue scaffold made of nanofibers has a loose and porous structure, it can provide sufficient nutrients for cell growth and remove metabolites in time. In addition, studies have shown that by adjusting the diameter, mechanical strength, orientation, and other factors of electrospun nanofibers, functions of the scaffold can be further promoted [48–51]. By including additives to the electrospun fiber, the scaffold can have other physical properties. For example, adding graphene to electrospun fiber can improve its conductivity to promote nerve tissue regeneration [46,49]. Currently, there has been little work done on the development of magnetic scaffolds by electrospinning and even less on preparing electrospun silk fibers with MNPs.

In this study, biocompatible M-type barium hexaferrite ($BaFe_{12}O_{19}$ or BaM) was added into the *B. Mori* silk fibroin protein, and fibers were produced by electrospinning [36,52–54]. The objective was to develop biocompatible magnetic composites whose properties could be modified to fit the material application. A comprehensive study was conducted to investigate the interaction between the magnetic inclusions and the protein matrix, measure their tunable mechanical, thermal, and magnetic properties, and analyze the magnetic field dependence of the cytotoxicity of these hybrid fibers with human embryonic kidney cells.

2. Materials and methods

2.1. Raw materials

Bombyx mori silk cocoons were purchased from Treenway Silks (Lakewood, CO, USA). Silk cocoons were firstly degummed by boiling in a 0.02 M $NaHCO_3$ (Sigma-Aldrich, St. Louis, MO, USA) solution for 30 min. Then the degummed fibers were rinsed three times in DI water to thoroughly remove the sericin coatings. The rinsed fibers were dried in a vacuum oven overnight. The following materials were used as purchased: M-type barium hexaferrite ($BaFe_{12}O_{19}$), Alfa Aesar (Haverhill, MA, USA); formic acid (ACS Grade 98%), EMD Millipore Corporation (Burlington, MA, USA); and anhydrous calcium chloride, AMRESCO Inc. (Solon, OH, USA).

2.2. Material synthesis

Dried silk fibroin (SF) fibers were dissolved in a formic acid solution with 4% w/v calcium chloride at a concentration of 0.15 g/mL. The SF solution was centrifuged to remove the impurities at 5000 rpm for 10 min. BaM was added to the solution in various weight ratios to the silk fibroin, including BaM/SF = 0 (0 wt% BaM), 1/20 (~4.8 wt% BaM), 1/10 (~9.1 wt% BaM), 1/4 (20 wt% BaM), 1/2 (~33 wt% BaM). The detailed synthesis formula was listed in Supplemental Table 1. The SF/BaM solution was shaken with a vortex mixer for 10 min. The thoroughly mixed BaM/SF solution was electrospun into nanofibers with an 18-kV applied voltage at room temperature and relative humidity between 45 and 65%. A syringe pump (Harvard Apparatus Model 22, Holliston, MA, USA) was used to control the solution flow rate at 15 μl/min. Electrospun samples were collected between two parallel metal plates lined with aluminum foil, placed at 4 cm from the needle tip (Supplemental Fig. 1). Collecting from the two parallel plates can help the solvent evaporate faster from the as-spun fibers and slightly improve the alignment of the fibers as compared to that of the pad collector [55]. In addition, free-standing fiber mesh samples can be collected directly. The fibers were then dried in a vacuum oven for 24 h.

Samples collected directly from the vacuum oven are called as-spun (AS) samples. Some as-spun (AS) samples were then annealed in DI water for 1 h to remove $CaCl_2$ residues and then dried in a vacuum oven for another 24 h, and these samples are designated water-annealed (WA) samples. To further check the impact of stretching on the alignment of the electrospun fibers, the AS 1/20 BaM/SF sample was stretched at 110%, 150%, and 200% ratio to its original length. The 100% (original length) 1/20 BaM/SF sample was used as a control. Stretched fibers were immediately fixed at two ends and held in DI water for 30 min and then dried in the vacuum oven for 24 h.

2.3. Surface morphology characterization

The electrospun fibers were imaged with a Leo 1530 VP scanning electron microscope (SEM) (Oberkochen, Germany). All samples were sputter-coated with gold before SEM imaging that was done with an accelerating voltage ranging between 10 and 20 kV.

2.4. Structure characterization

A Bruker Tensor 27 Fourier-transform infrared (FTIR) spectrometer (Billerica, MA, USA) was used to investigate the structural information of the electrospun fibers. The spectrometer is equipped with a deuterated triglycine sulfate detector and a multiple reflection, horizontal MIRacle ATR attachment with a Ge crystal (Pike Tech, Madison, WI, USA). Experiments were conducted while continuously purging with nitrogen gas. The spectra were taken at a range of 4,000 to 400 cm^{-1} with 64 background scans and 64 sample scans at a resolution of 4 cm^{-1}. Each sample was characterized at three different spots to ensure homogeneity, and the obtained spectra were then all normalized. The Fourier self-deconvolution (FSD) was conducted as reported previously [56].

A Panalytical Empyrean x-ray diffractometer (Almelo, The Netherlands) equipped with a Pixel detector was used to investigate the crystal structure of the magnetic inclusions. Samples were measured with a custom-built fixture for x-ray diffraction and wide-angle x-ray scattering measurements. The generator was set to 45 kV and 40 mA, and the incident beam optic was a parallel-beam x-ray mirror with a 1/16° divergence slit.

2.5. Thermal stability characterization

Thermogravimetric analysis of BaM/SF electrospun fibers was carried out with the TA Instruments Q600 SDT Analyzer (Wilmington, DE, USA). The experiment was conducted with a continuous nitrogen gas flow rate of 50 mL/min, and each specimen weighed between 5 and 10 mg. Measurements were made from 30 °C to 800 °C at a heating rate of 10 °C/min.

2.6. Mechanical testing

Mechanical properties of samples were characterized with an EZ tensile tester (Shimadzu, Kyoto, Japan). The electrospun fiber mesh was cut into a rectangular shape with a length 40 mm and a width 5 mm. The average thickness of the electrospun fiber mesh was around 0.1 mm. Each end of the sample was fixed with adhesive tape that was then placed between the test clamps. The mounted sample was aligned in the vertical direction. Tensile tests were executed at 5 mm/min until specimen failure. A 10 N force sensor was used for the characterization. The cross-sectional area of the specimen was used to calculate the stress and Young's modulus (E) of the electrospun fiber mesh from the following equation:

$$E = \frac{\sigma}{\varepsilon} = \frac{F/A}{dl/l}$$

where σ is the tensile stress, ε is the tensile strain, F is the applied force, A is the cross-section area of the sample, dl is the change in length, l is the original length of the sample. There are at least three parallel tests for each group of samples.

2.7. Magnetic characterization

A vibrating sample magnetometer (VSM) probe with a Physical Property Measurement System (Quantum Design, San Diego, CA, USA) was used to measure the magnetic properties. The experiment was performed at room temperature with magnetic fields up to 4 T. The procedure of measurements is summarized in Supplemental Fig. 2.

2.8. Biocompatibility study

The mesh of the annealed samples ($n = 8$ per set) was cut into disc shapes of the same size as the culture plate wells and placed into 96-well tissue culture plates. The samples were first sterilized with UV light for 24 h before adding the cell culture medium (Dulbecco's modified Eagle's medium; HyClone, with 4.00 mM L-glutamine and 4500 mg/L glucose), supplemented with 10% fetal bovine serum (Life Technologies Inc.) and 100 U/mL Penicillin-Streptomycin (Thermo Fisher Scientific Inc., USA). After 12 h, human embryonic kidney cells (HEK293) from ATCC (American Type Culture Collection) were plated into the 96-well plate. Two sets of cell studies were performed: One set of experiments was performed within a magnetic field of 1 T, and the other set was performed without an external magnetic field. Cells cultured in the blank wells of the plate with or without magnetic field were used as controls, respectively. After incubating the cells in an atmosphere of 95% air, 5% CO_2, at 37 °C for 48 h, cell numbers were acquired with a 3-[4,5-dimethylthiazole-2-yl]-2,5-diphenyltetrazolium bromide (MTT) assay.

3. Results and discussion

3.1. Morphology analysis

The morphology and fiber diameter of the magnetic nanofibers were characterized by SEM (Fig. 1). All AS samples showed smooth and uniform surfaces (Fig. 1a, d, g and j) for BaM/SF = 0, 1/20, 1/10, and 1/4; however, the AS 1/2 BaM/SF samples had a rougher surface (Fig. 1m) due to the high content (~12 vol%) of BaM nanoparticles in the SF matrix. In the AS 1/2 BaM/SF sample, more BaM particles can be found on the fiber surfaces, and the length of the fibers also decreased compared with low BaM content samples. It was reported that the incorporated content ratio could change the viscoelasticity of the mixed solution, as well as the surface tension of the droplets formed [57]. In this case, when the BaM content is high, the viscoelasticity of the mixed solution is low, and thus discontinuous fibers were formed. The AS 0 (pure SF) sample had the largest fiber diameter with a size distribution centered around 2 μm (Fig. 1b), while all other AS samples showed a smaller diameter with an average diameter of 1.6 μm or less (Fig. 1e, h, k, n), suggesting substantial interaction between the protein and the inclusions during the fiber formation. Aziz et al. [58] reported the diameter of electrospun SF fiber ranged from 0.1 to 1.2 μm, which is much thinner than that of ours. This might be caused by the higher injection rate and higher humidity while we were fabricating our electrospun SF fibers. In comparison, electrospun water-annealed (WA) fibers (Fig. 1c, f, I, and o) were completely physically cross-linked by the β-sheet crystals in the silk proteins (see section 3.2), unlike the overlapping pattern of the AS samples or other electrospun synthetic polymer nanofibers [59–61]. Generally, all WA samples showed a dense mat-like pattern of fibers embedded within a matrix. Basically, water annealing caused the fibers to be closer to each other with smaller scaffold pores, although the alignment remained unchanged.

3.2. Structural analysis

FTIR spectroscopy was performed to characterize the effects of BaM content and water annealing treatment on the secondary structures of SF proteins (Fig. 2). All AS samples showed a similar pattern in the amide I region, with a peak centered around 1640 cm^{-1} for AS 0 (pure SF) fibers that slightly shifted to 1643 cm^{-1} for AS 1/2 BaM/SF fibers, which indicates that the structure of AS fibers was dominated by random coils. In the amide II region, AS samples showed a peak centered around 1540 cm^{-1} with a shoulder around 1514 cm^{-1}, which typically suggests a loose side-chain group in the protein matrix [43,44,62,63]. In comparison, the amide I peak of the WA samples all shifted to around 1621 cm^{-1}, indicating a predominant β-sheet crystal structure. In the amide II region, the peak at 1540 cm^{-1} disappeared while the peak at 1514 cm^{-1} became sharp, suggesting a tightly packed protein matrix with side-chain groups such as tyrosines outside the protein backbones [43,44].

More quantitative analysis of the secondary structure content was done with a Fourier self-deconvoluted curve fitting method [56,64] (Fig. 2c and d, and Supplemental Fig. 3). It shows that the β-sheet content of the AS samples was around 20% and probably dominated by intramolecular beta sheets [29–31]. The β-sheet content of the WA samples was about 35–38%, with perhaps a small decrease with BaM content. It has been well established that water annealing can induce the formation of β-sheet crystalline structure in SF [43], which could play the role of crosslinkers to encapsulate the nanoparticles in the protein matrix. It was also

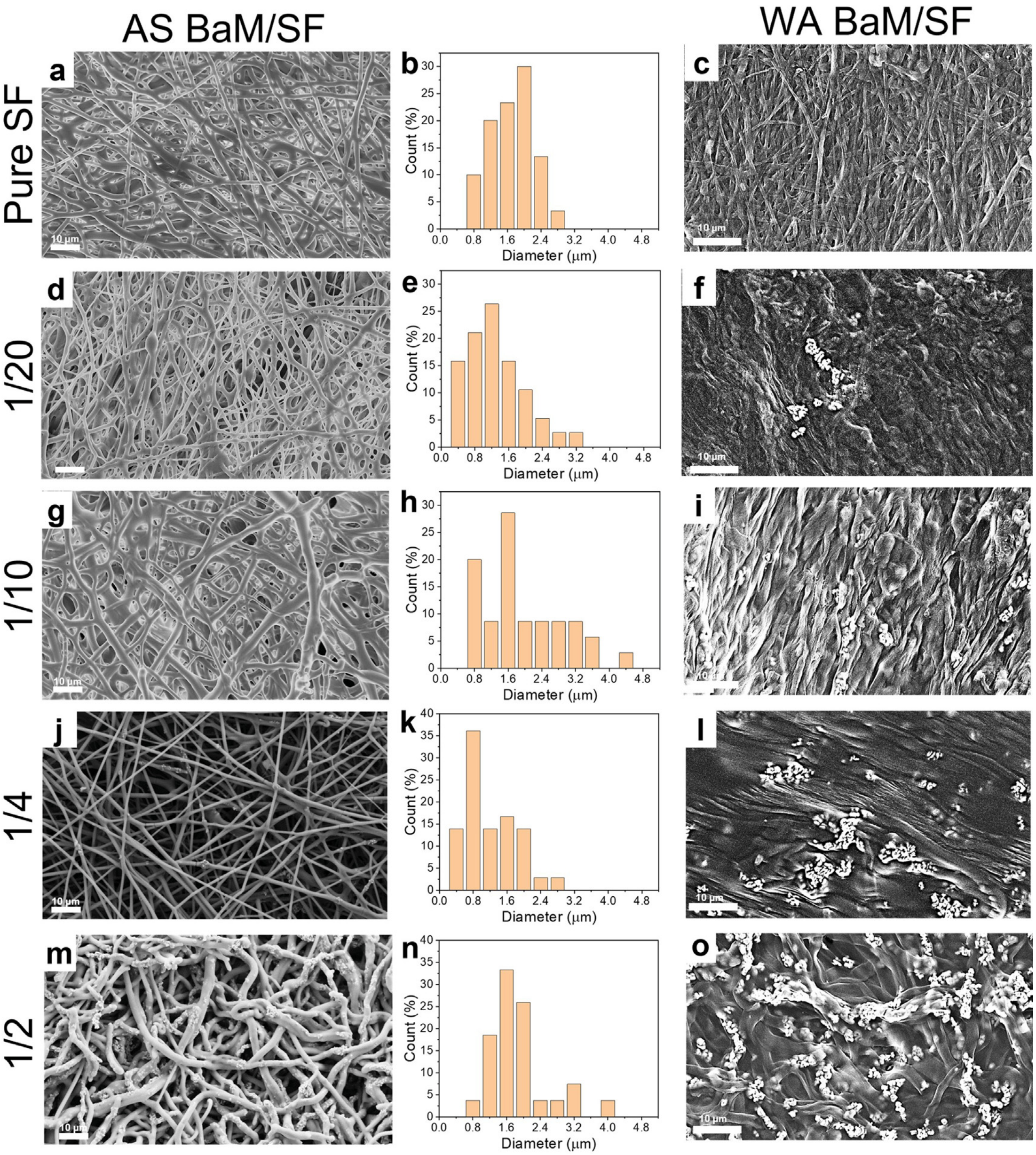

Fig. 1. SEM images of as-spun (AS) fibers, diameter distribution of as-spun (AS) fibers, and SEM images of water-annealed (WA) fibers, respectively, for BaM/SF = 0 (a–c), 1/20 (d–f), 1/10 (g–i), 1/4 (j–l), and 1/2 (m–o). The scale bar for all the images is 10 μm.

found that random coils content of AS fibers was about 42% and decreased to about 30% after annealing.

Further structural study was done by x-ray diffraction (Supplemental Fig. 4). For the 1/20 BaM/SF sample, there was no detectable signal aside from that of the silk. At larger concentrations, the BaM signal becomes apparent. No other peaks were identified besides those of silk and BaM. The hexagonal unit cell of BaM was refined to $a = 5.8883 \pm 0.0004$ Å and $c = 23.176 \pm 0.002$ Å, agreeing quite closely with the reference values of $a = 5.889$ Å and $c = 23.182$ Å (JCPDS card 98-000-2772), confirming that the phase is stoichiometric. It is known that hexagonal ferrites are line compounds, and deviation from stoichiometric leads to additional phases, which were not observed [65–69]. From the Scherrer equation, the particle sizes were estimated to be 80 ± 20 nm from the measured peak widths.

3.3. *Thermal stability analysis*

Thermal stability was characterized by TGA (Fig. 3), and the thermal properties are summarized in Table 1. For the AS 0 (pure SF) sample, a 16.3% weight loss was found at 173 °C due to the evaporation of bound water in contrast to 5.9% weight loss found in the WA 0 (pure SF) sample at the same temperature. This difference is probably due to the $CaCl_2$ residues and the larger content of random coils in the AS samples, which can maintain more bound water molecules in the matrix. All AS samples showed a small degradation around 220 °C (T_{d1}) and a major degradation around 310 °C (T_{d2}). In comparison, the water annealed pure SF sample only showed a significant degradation peak around 267 °C (T_{d2}), indicating that the silk proteins were tightly bounded with the BaM nanoparticles after the water annealing treatment, and thus only

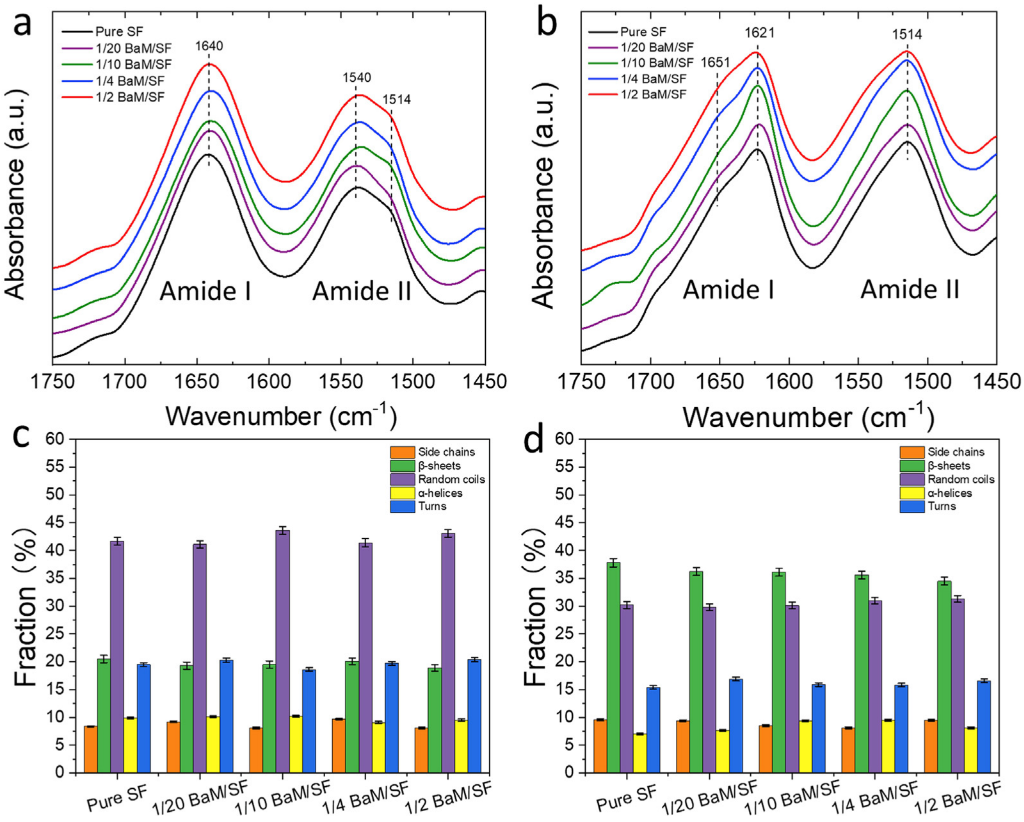

Fig. 2. FTIR spectra of (a) AS and (b) WA fibers. Secondary structure contents of (c) AS and d) WA fibers. Note that the secondary structure content depends strongly on processing but is effectively independent of BaM content with AS fibers containing mostly random coils and WA dominated by β-sheet crystals.

one major degradation from the composites was observed. For WA samples with more than 5% BaM nanoparticles, there is an additional degradation peak (T_{d3}) near 700 °C, which is absent in the AS samples. This may indicate that some parts of water-annealed composites with strong molecular interactions are so stable that they decompose only at high temperatures. The residual weight of AS samples at 800 °C is between 35 and 38%, while the residual weight of WA samples generally increases with BaM content, which again suggest that the water annealing process improves the thermal stability of the fibers.

3.4. Mechanical properties

Results of the stress-strain tensile test are shown in Fig. 4 and are summarized in Fig. 5. The ultimate strength of AS samples gradually decreased from the maximum for pure SF (~1 GPa) (Fig. 5b) while Young's modulus of all AS samples was similar (Fig. 5a), both results being attributed to the weak bonding between the SF matrix and the BaM inclusions before annealing. This was in accord with the smaller diameter of the AS fibers when BaM was incorporated. On the other hand, for WA composites, while the WA 0 (pure SF) sample showed the highest ultimate strength (~1 GPa), it also had the lowest value for Young's modulus (1.0 GPa). As expected for composites with strong interfacial bonding, Young's modulus of the WA samples increased with BaM content. The AS samples generally showed a much higher strain elongation ratio (1.5–2 times) than that of their WA counterparts (Fig. 5c), which indicates that the annealed samples may lose some flexibility of the materials due to the high crystallinity. The average strain ratio of the WA samples was in the range of 45%–55%.

As discovered in the mechanical study, Young's modulus of the AS samples is very small, and their strain ratios can be quite large. To further investigate the effect of stretching on the electrospun fiber alignments, AS 1/20 BaM/SF samples were stretched to different ratios (Fig. 6), and the ends were fixed while the sample was annealed in deionized water. As the draw ratio increased, the alignment of the fiber improved (Fig. 6a–d) so that at an elongation of 100% (200% of the original length), the fibers became parallel to each other (Fig. 6d). Natural silk fibroin consists of a large proportion of α-amino acids, glycine, alanine, and serine [70,71], and the water molecule functions as plasticizer while the stretched fibers are annealed in water, giving the amorphous part of the fiber much higher mobility [43,72,73]. Therefore, stretching further improves the alignment of the fibers, while the water annealing procedure can fix the alignment of the fibers.

3.5. Magnetic properties

All BaM-containing samples showed typical ferromagnetic behavior (Fig. 7) with a coercive field H_c of about 3 kOe (Fig. 7a and b). The dependence of the saturation magnetization M_s on the weight fraction of BaM is shown in Fig. 7c. Values of M_s, H_c, and remanent magnetization M_r for pure SF, BaM, and the composite fibers are listed in Table 2. The present M_s and H_c values of BaM are close to those reported by Pattanayak et al. [74]. While finite-size effects can be important in ferromagnets [75,76], the present nanoparticles are significantly larger than those in the critical regime, which occurs for particles smaller than 20 nm [77]. Assuming that there were no changes in the magnetic properties of the BaM due to processing, the M_s value of the composite should be

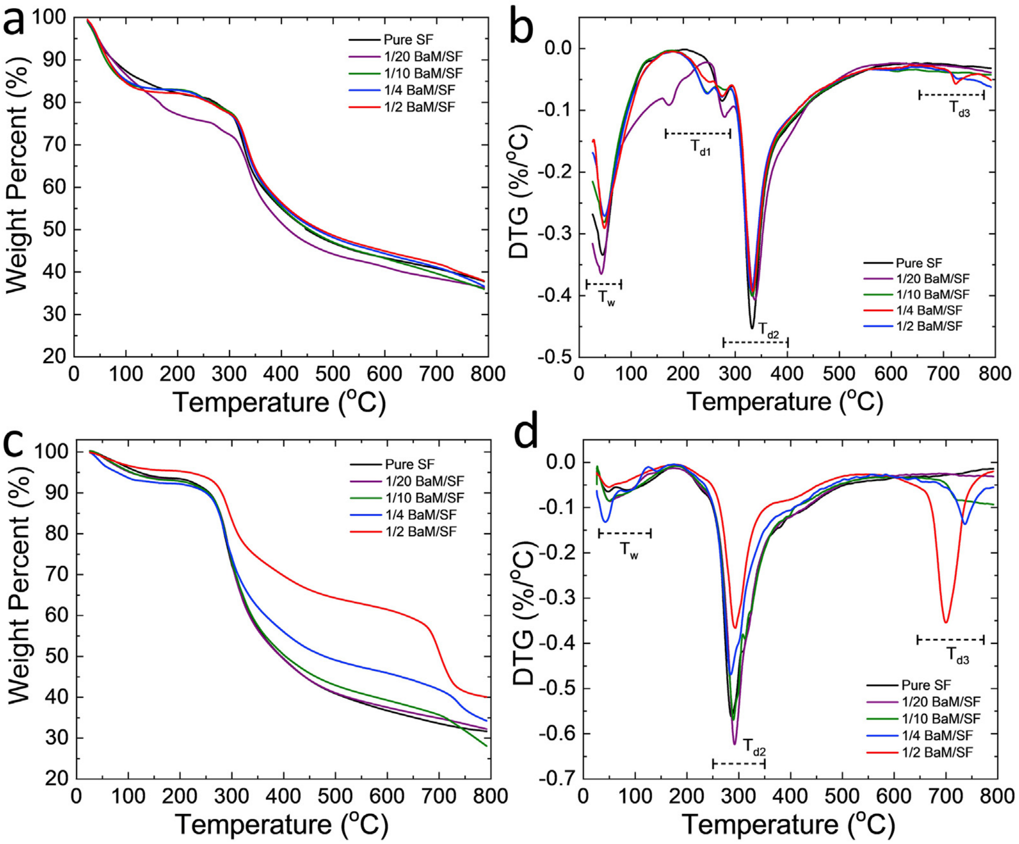

Fig. 3. a) and (b) display the thermogravimetric curves of as-spun fibers and water-annealed fibers, respectively. (c) and (d) display the 1st derivative TG (DTG) curves of as-spun fiber and water-annealed fibers, respectively.

Table 1
Thermal properties of AS and WA electrospun fibers.

	T_w (°C)	T_{d1} (°C)	T_{d2} (°C)	T_{d3} (°C)
Pure SF	58	267	318	–
1/20 BaM/SF	47	265	311	–
1/10 BaM/SF	66	224	317	–
1/4 BaM/SF	81	223	315	–
1/2 BaM/SF	77	227	318	716
WA Pure SF	34	–	263	–
WA 1/20 BaM/SF	38	–	270	–
WA 1/10 BaM/SF	39	–	267	708
WA 1/4 BaM/SF	33	–	262	707
WA 1/2 BaM/SF	36	–	269	676

about 69× emu/g, where x is the weight fraction of BaM since silk will not contribute to M_s as it contains no magnetic ions. Note that there is a linear relationship between the weight fraction and M_s, except the line does not go through the origin but has a horizontal intercept at 4 wt%. Presumably, some of the BaM nanoparticles dissolved in the silk solution, saturating at about 4 wt% with the remaining BaM nanoparticles left intact. This is consistent with the diffraction studies that showed only tiny measurable BaM for the 1/20 BaM/SF sample (note the sensitivity of x-ray diffraction to phase identification is normally about 1–2 wt%). After water annealing, the nanofibers retained their magnetic properties (Fig. 7c). Since BaM is a hard ferromagnet, the strong permanent magnetic

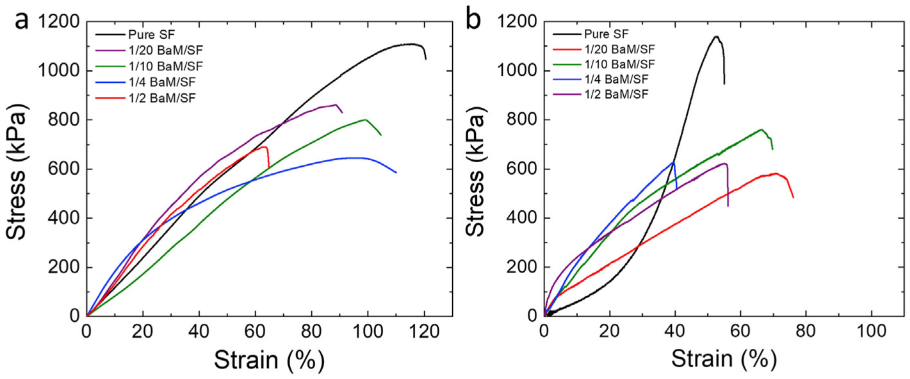

Fig. 4. Representative stress-strain curves of (a) AS and (b) WA fibers.

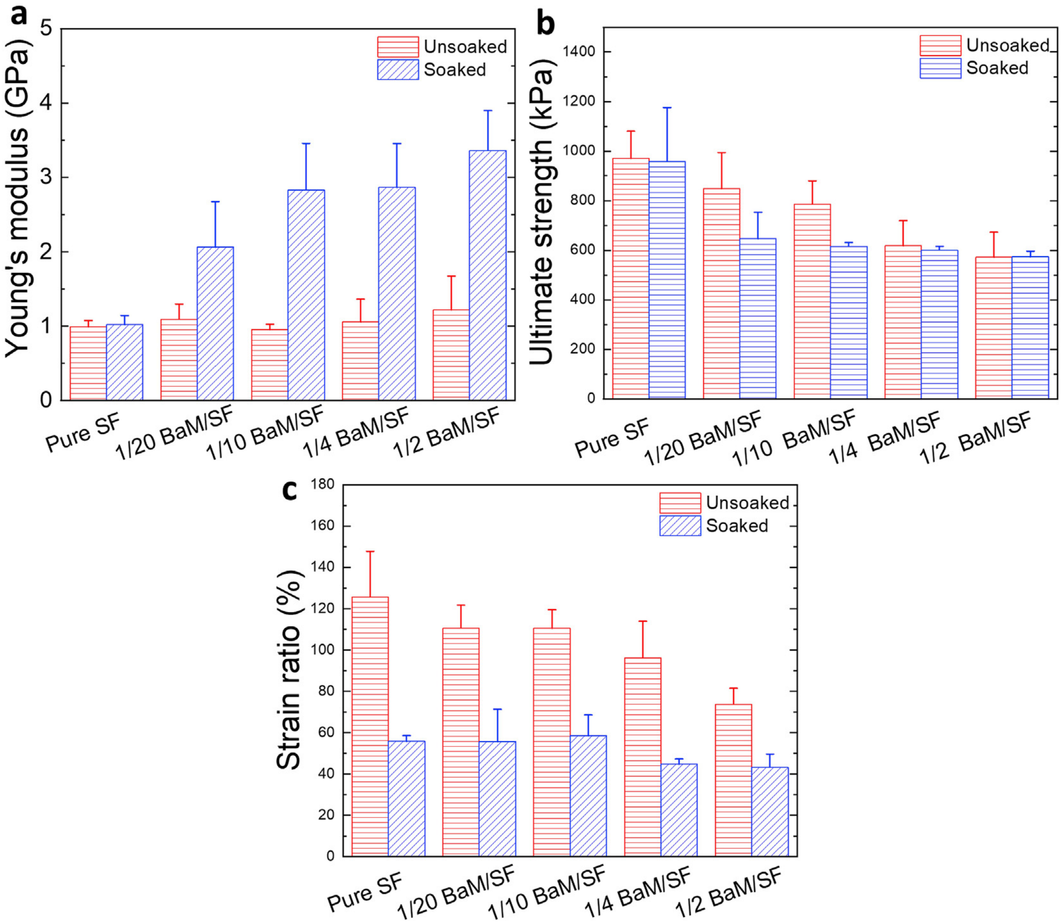

Fig. 5. (a) Young's modulus, (b) ultimate strength, and (c) strain ratio of AS and WA fibers.

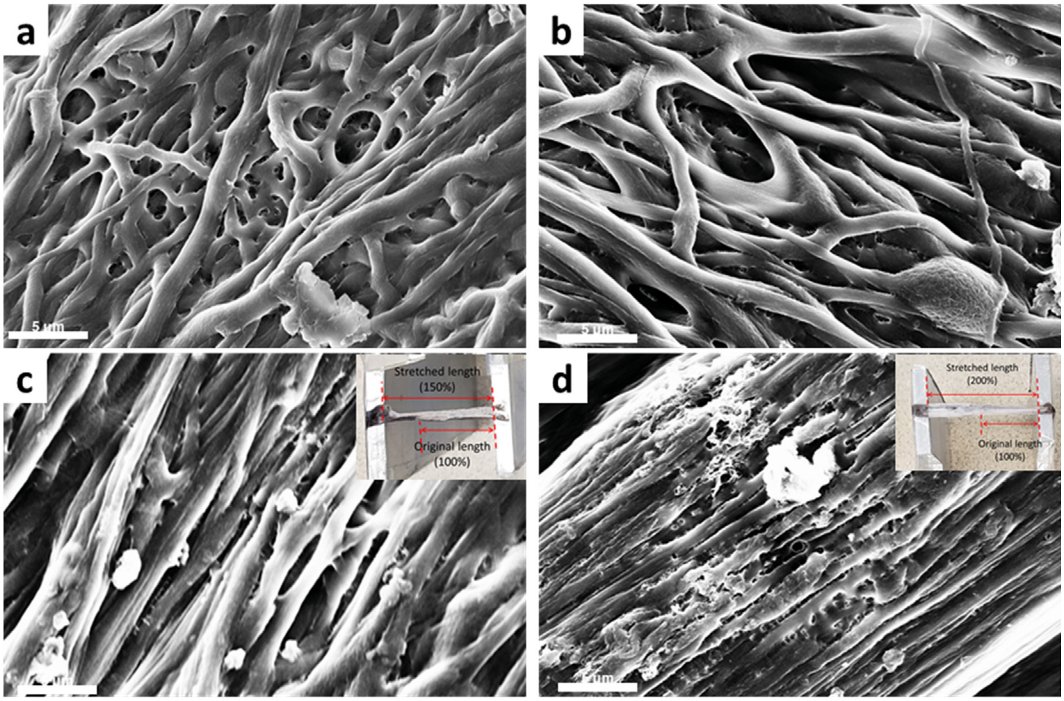

Fig. 6. SEM images of stretched and water-annealed 1/20 BaM/SF nanofiber sample: (a) 100% (original fiber), (b) 110%, (c) 150%, and (d) 200% of the original length; The inset graph in 3c and 3d show the 150% and 200% stretching setup, respectively; the scale bar is 5 μm.

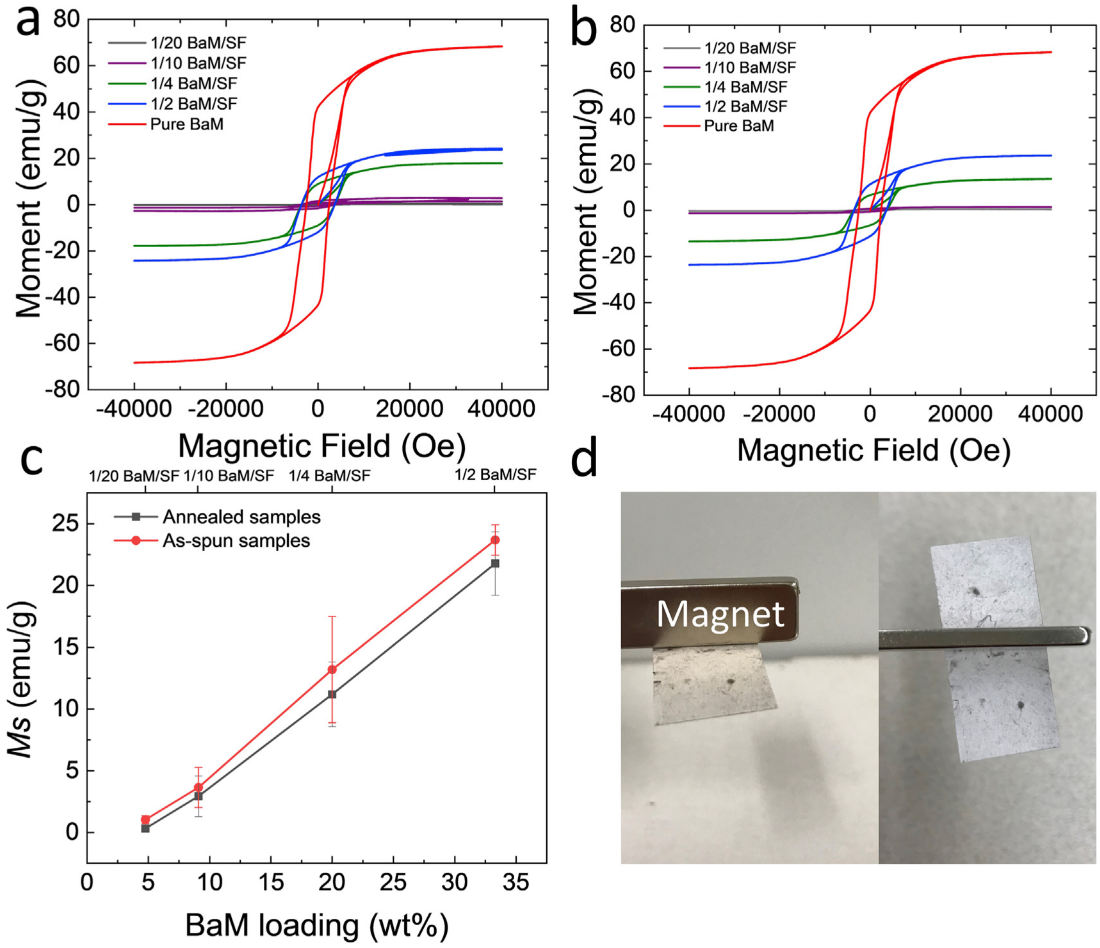

Fig. 7. Magnetization and hysteresis loops of (a) AS and (b) WA fiber samples at room temperature. (c) Saturation moment of AS and WA BaM/SF nanofibers as a function of the magnetic particle content. (d) Photos of an AS 1/4 BaM/SF mesh attracted to a magnet.

Table 2
Magnetic properties of the as-spun fibers and water-annealed fibers.

Sample	As-spun fibers			Water-annealed fibers		
	M_s (emu/g)	M_r (emu/g)	H_c (kOe)	M_s (emu/g)	M_r (emu/g)	H_c (kOe)
Pure SF	0	0	0	0	0	0
1/20 BaM/SF	1.04 ± 0.32	0.09 ± 0.01	3.40 ± 0.03	0.33 ± 0.06	0.22 ± 0.01	3.23 ± 0.03
1/10 BaM/SF	3.64 ± 1.62	1.58 ± 0.09	3.57 ± 0.02	2.94 ± 1.65	0.69 ± 0.02	3.52 ± 0.04
1/4 BaM/SF	13.2 ± 4.3	8.95 ± 0.08	3.61 ± 0.03	11.2 ± 2.6	6.51 ± 0.05	3.63 ± 0.02
1/2 BaM/SF	23.7 ± 1.2	11.9 ± 0.11	3.63 ± 0.02	21.8 ± 2.6	11.21 ± 0.07	3.60 ± 0.03
Pure BaM	69.0 ± 2.4	42.2 ± 0.31	2.15 ± 0.11	69.0 ± 2.4	42.2 ± 0.31	2.15 ± 0.11

moment maintained by the composites makes for consideration in the use of biomedical applications such as magnetic thermotherapy and tissue engineering (Fig. 7d).

3.6. Biocompatibility analysis

WA fiber meshes were placed into cell culture plates, seeded with human embryonic kidney cells (HEK293) for *in vitro* biocompatibility study. Since the culture medium was water-based, AS samples would be transformed to the WA samples during the multiday cell study, and thus, they were not tested separately. The control group with no external magnetic field shows an optical density (OD) of cells about 0.29, which is within the margin of error of the value for the control group with an external magnetic field (Fig. 8). Compared to the control, pure silk nanofibers promoted cell growth significantly (Fig. 8) since the porous 3D structure of the mesh provided more space for cells to proliferate. In the absence of a magnetic field, cell growth increased slightly with increasing BaM content (Fig. 8), indicating that the composite system is non-cytotoxic to human cells and biocompatible for various medical applications. However, when the field was applied, there was enhanced cell growth in samples with BaM, and that was most significant for the WA 1/20 and WA 1/10 samples.

We propose the following mechanism for BaM/SF composites (Fig. 9): the initial AS fibers are dominated by random coils (Fig. 9a), which have weak interaction with the BaM nanoparticles; after water annealing, the magnetic nanoparticles were encapsulated into the protein matrix due to the formation of β-sheet crystals as

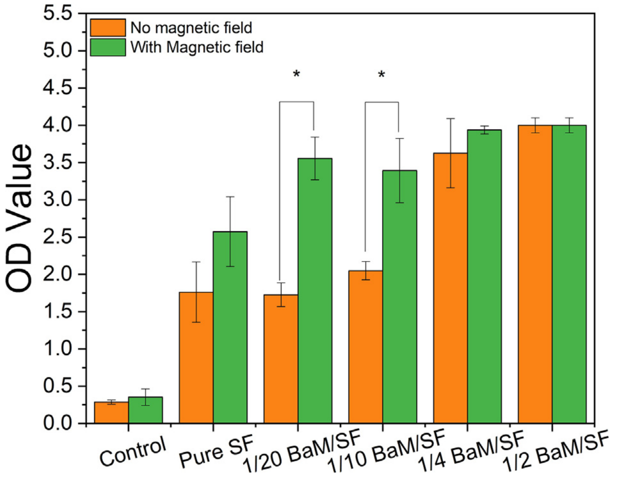

Fig. 8. Comparison of cell viability of HEK293T cells cultured on the blank control, pure SF, and BaM/SF hybrid fibers with or without an external magnetic field. The t-tests were performed between indicated groups (*: $p < 0.01$).

crosslinkers (Fig. 9b), and both the thermal stability and mechanical strength of the fibers were enhanced; under the influence of an external magnetic field, the fiber matrix can further promote cell proliferation and provide cells with more vitality during migration and proliferation in the scaffold matrix (Fig. 9c).

4. Conclusion

This study investigated the structure, physical properties, and cytotoxicity of silk fibroin-barium hexaferrite composite fibers produced by electrospinning. Through a water-annealing method, the physical properties of the fiber materials were significantly altered due to an increase in β-sheet crystallinity. The treatment led to increased mechanical strength and thermal stability of the material. In all cases, the magnetism of the barium hexaferrite was maintained. The cytotoxicity was low, and the magnetic inclusions in the fibers led to mechanical deformation during the application of the magnetic field, which promoted the growth of human cells on the surface. Such materials provide great potential for use in a wide range of biomedical applications.

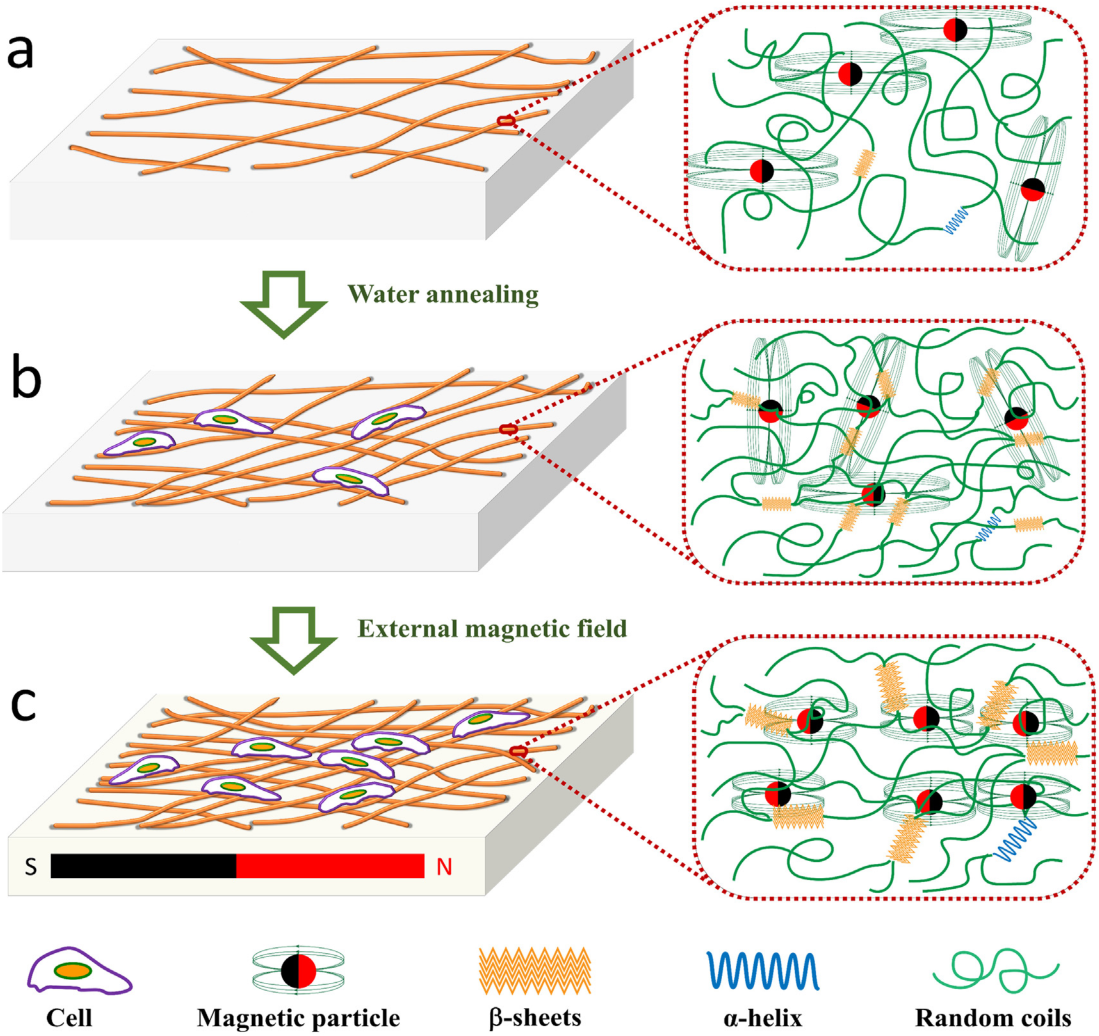

Fig. 9. Mechanism of silk-BaM magnetic materials. (a) As-spun BaM/SF fibers are dominated by random coils; (b) after water annealing, the magnetic nanoparticles were further encapsulated into the protein matrix due to the formation of β-sheet crystals as crosslinkers; (c) by adding an external magnetic field, the proliferation of human cells on the annealed magnetic nanofiber matrix can be further enhanced.

CRediT authorship contribution statement

Ye Xue: Formal analysis, Validation, Investigation, Writing - original draft, Visualization. **Krista Jackson:** Investigation, Data curation, Writing - original draft. **Natalie Page:** Investigation, Data curation. **Xiaoyang Mou:** Investigation, Data curation, Formal analysis. **Samuel Lofland:** Conceptualization, Methodology, Writing - review and editing, Resources. **Xiao Hu:** Conceptualization, Methodology, Validation, Supervision, Project administration, Formal analysis, Funding acquisition, Writing - original draft, review and editing, Resources.

Declaration of competing interest

The authors declare that they have no known competing financial interests or personal relationships that could have appeared to influence the work reported in this paper.

Acknowledgment

This study was supported by the Rowan University Start-up Grants. X.H. is also supported by NSF Biomaterials Program (DMR-1809541) and Future Manufacturing Program (CMMI-2037097).

Appendix A. Supplementary data

Supplementary data to this article can be found online at https://doi.org/10.1016/j.mtchem.2021.100570.

References

[1] J. Gao, H. Gu, B. Xu, Multifunctional magnetic nanoparticles: design, synthesis, and biomedical applications, Acc. Chem. Res. 42 (8) (2009) 1097–1107.

[2] N.S. Satarkar, J.Z. Hilt, Hydrogel nanocomposites as remote-controlled biomaterials, Acta Biomater. 4 (1) (2008) 11–16.

[3] M. Rahimi, A. Wadajkar, K. Subramanian, M. Yousef, W. Cui, J.-T. Hsieh, K.T. Nguyen, In vitro evaluation of novel polymer-coated magnetic nanoparticles for controlled drug delivery, Nanomed. Nanotechnol. Biol. Med. 6 (5) (2010) 672–680.

[4] Q.A. Pankhurst, J. Connolly, S.K. Jones, J. Dobson, Applications of magnetic nanoparticles in biomedicine, J. Phys. D Appl. Phys. 36 (13) (2003) R167.

[5] T. Kobayashi, Cancer hyperthermia using magnetic nanoparticles, Biotechnol. J. 6 (11) (2011) 1342–1347.

[6] M. Bañobre-López, A. Teijeiro, J. Rivas, Magnetic nanoparticle-based hyperthermia for cancer treatment, Rep. Practical Oncol. Radiother. 18 (6) (2013) 397–400.

[7] J.L. Corchero, A. Villaverde, Biomedical applications of distally controlled magnetic nanoparticles, Trends Biotechnol. 27 (8) (2009) 468–476.

[8] J.B. Haun, T.J. Yoon, H. Lee, R. Weissleder, Magnetic nanoparticle biosensors, Wiley Interdiscipl. Rev.: Nanomed. Nanobiotechnol. 2 (3) (2010) 291–304.

[9] L.H. Reddy, J.L. Arias, J. Nicolas, P. Couvreur, Magnetic nanoparticles: design and characterization, toxicity and biocompatibility, pharmaceutical and biomedical applications, Chem. Rev. 112 (11) (2012) 5818–5878.

[10] S. Gil, C.R. Correia, J.F. Mano, Magnetically labeled cells with surface-modified Fe3O4 spherical and rod-shaped magnetic nanoparticles for tissue engineering applications, Adv. Health. Mater. 4 (6) (2015) 883–891.

[11] N. Bock, A. Riminucci, C. Dionigi, A. Russo, A. Tampieri, E. Landi, V.A. Goranov, M. Marcacci, V. Dediu, A novel route in bone tissue engineering: magnetic biomimetic scaffolds, Acta Biomater. 6 (3) (2010) 786–796.

[12] A. Tampieri, M. Iafisco, M. Sandri, S. Panseri, C. Cunha, S. Sprio, E. Savini, M. Uhlarz, T. Herrmannsdörfer, Magnetic bioinspired hybrid nanostructured collagen–hydroxyapatite scaffolds supporting cell proliferation and tuning regenerative process, ACS Appl. Mater. Interfaces 6 (18) (2014) 15697–15707.

[13] S.K. Samal, V. Goranov, M. Dash, A. Russo, T. Shelyakova, P. Graziosi, L. Lungaro, A. Riminucci, M. Uhlarz, M. Bañobre-López, Multilayered magnetic gelatin membrane scaffolds, ACS Appl. Mater. Interfaces 7 (41) (2015) 23098–23109.

[14] S. Gil, J.F. Mano, Magnetic composite biomaterials for tissue engineering, Biomaterials Science 2 (6) (2014) 812–818.

[15] K. Ulbrich, K. Hola, V. Subr, A. Bakandritsos, J. Tucek, R. Zboril, Targeted drug delivery with polymers and magnetic nanoparticles: covalent and non-covalent approaches, release control, and clinical studies, Chem. Rev. 116 (9) (2016) 5338–5431.

[16] E.J. Bealer, K. Kavetsky, S. Dutko, S. Lofland, X. Hu, Protein and polysaccharide-based magnetic composite materials for medical applications, Int. J. Mol. Sci. 21 (1) (2020) 186.

[17] D. Vinnik, A.Y. Starikov, V. Zhivulin, K. Astapovich, V. Turchenko, T. Zubar, S. Trukhanov, J. Kohout, T. Kmječ, O. Yakovenko, Structure and magnetodielectric properties of titanium substituted barium hexaferrites, Ceram. Int. 47 (12) (2021) 17293–17306.

[18] V. Turchenko, V. Kostishin, S. Trukhanov, F. Damay, M. Balasoiu, B. Bozzo, I. Fina, V.V. Burkhovetsky, S. Polosan, M. Zdorovets, Structural features, magnetic and ferroelectric properties of SrFe10. 8In1. 2O19 compound, Mater. Res. Bull. 138 (2021) 111236.

[19] A. Thakur, N. Sharma, M. Bhatti, M. Sharma, A.V. Trukhanov, S.V. Trukhanov, L.V. Panina, K.A. Astapovich, P. Thakur, Synthesis of barium ferrite nanoparticles using rhizome extract of Acorus calamus: characterization and its efficacy against different plant phytopathogenic fungi, Nano-Structures & Nano-Objects 24 (2020) 100599.

[20] A. Kozlovskiy, D. Shlimas, M. Zdorovets, Synthesis, structural properties and shielding efficiency of glasses based on TeO 2-(1-x) ZnO-xSm 2 O 3, J. Mater. Sci. Mater. Electron. 32 (9) (2021) 12111–12120.

[21] D. Vinnik, V. Zhivulin, D. Sherstyuk, A.Y. Starikov, P. Zezyulina, S. Gudkova, D. Zherebtsov, K. Rozanov, S. Trukhanov, K. Astapovich, Electromagnetic properties of zinc–nickel ferrites in the frequency range of 0.05–10 GHz, Materials Today Chemistry 20 (2021) 100460.

[22] M. Zdorovets, A. Kozlovskiy, D. Shlimas, D. Borgekov, Phase transformations in FeCo–Fe2CoO4/Co3O4-spinel nanostructures as a result of thermal annealing and their practical application, J. Mater. Sci. Mater. Electron. (2021) 1–12.

[23] T. Dippong, O. Cadar, I.G. Deac, M. Lazar, G. Borodi, E.A. Levei, Influence of ferrite to silica ratio and thermal treatment on porosity, surface, microstructure and magnetic properties of Zn0. 5Ni0. 5Fe2O4/SiO2 nanocomposites, J. Alloys Compd. 828 (2020) 154409.

[24] T. Dippong, E.-A. Levei, I.G. Deac, F. Goga, O. Cadar, Investigation of structural and magnetic properties of NixZn1-xFe2O4/SiO2 (0≤ x≤ 1) spinel-based nanocomposites, J. Anal. Appl. Pyrol. 144 (2019) 104713.

[25] T. Dippong, E.A. Levei, I.G. Deac, E. Neag, O. Cadar, Influence of cu2+, ni2+, and zn2+ ions doping on the structure, morphology, and magnetic properties of co-ferrite embedded in sio2 matrix obtained by an innovative sol-gel route, Nanomaterials 10 (3) (2020) 580.

[26] T. Dippong, I.G. Deac, O. Cadar, E.A. Levei, I. Petean, Impact of Cu2+ substitution by Co2+ on the structural and magnetic properties of CuFe2O4 synthesized by sol-gel route, Mater. Char. 163 (2020) 110248.

[27] D. Tishkevich, I. Korolkov, A. Kozlovskiy, M. Anisovich, D. Vinnik, A. Ermekova, A. Vorobjova, E. Shumskaya, T. Zubar, S. Trukhanov, Immobilization of boron-rich compound on Fe3O4 nanoparticles: stability and cytotoxicity, J. Alloys Compd. 797 (2019) 573–581.

[28] M. Almessiere, A. Trukhanov, F. Khan, Y. Slimani, N. Tashkandi, V. Turchenko, T. Zubar, D. Tishkevich, S. Trukhanov, L. Panina, Correlation between microstructure parameters and anti-cancer activity of the [Mn0. 5Zn0. 5](EuxNdxFe2-2x) O4 nanoferrites produced by modified sol-gel and ultrasonic methods, Ceram. Int. 46 (6) (2020) 7346–7354.

[29] D. Jao, Y. Xue, J. Medina, X. Hu, Protein-based drug-delivery materials, Materials 10 (5) (2017) 517.

[30] Y. Xue, D. Jao, W. Hu, X. Hu, Silk-silk blend materials, J. Therm. Anal. Calorim. 127 (1) (2017) 915–921.

[31] Y. Xue, F. Wang, M. Torculas, S. Lofland, X. Hu, Formic acid regenerated mori, tussah, eri, Thai, and muga silk materials: mechanism of self-assembly, ACS Biomater. Sci. Eng. 5 (12) (2019) 6361–6373.

[32] E.J. Bealer, S. Onissema-Karimu, A. Rivera-Galletti, M. Francis, J. Wilkowski, D. Salas-de la Cruz, X. Hu, Protein–polysaccharide composite materials: fabrication and applications, Polymers 12 (2) (2020) 464.

[33] K.A. Callaway, Y. Xue, V. Altimari, G. Jiang, X. Hu, Comparative investigation of thermal and structural behavior in renewably sourced composite films of even-even nylons (610 and 1010) with silk fibroin, Polymers 10 (9) (2018) 1029.

[34] H. Han, H. Ning, S. Liu, Q. Lu, Z. Fan, H. Lu, G. Lu, D.L. Kaplan, Silk biomaterials with vascularization capacity, Adv. Funct. Mater. 26 (3) (2016) 421–432.

[35] Z. Zhou, S. Zhang, Y. Cao, B. Marelli, X. Xia, T.H. Tao, Engineering the future of silk materials through advanced manufacturing, Adv. Mater. 30 (33) (2018) 1706983.

[36] D.A. Brennan, A.A. Conte, G. Kanski, S. Turkula, X. Hu, M.T. Kleiner, V. Beachley, Mechanical considerations for electrospun nanofibers in tendon and ligament repair, Advanced healthcare materials 7 (12) (2018) 1701277.

[37] M. Torculas, J. Medina, W. Xue, X. Hu, Protein-based bioelectronics, ACS Biomater. Sci. Eng. 2 (8) (2016) 1211–1223.

[38] S. Ling, Z. Qin, C. Li, W. Huang, D.L. Kaplan, M.J. Buehler, Polymorphic regenerated silk fibers assembled through bioinspired spinning, Nat. Commun. 8 (1) (2017) 1–12.

[39] I. Su, M.J. Buehler, Spider silk: dynamic mechanics, Nat. Mater. 15 (10) (2016) 1054–1055.

[40] F. Wang, H. Wu, V. Venkataraman, X. Hu, Silk fibroin-poly (lactic acid) biocomposites: effect of protein-synthetic polymer interactions and miscibility on material properties and biological responses, Mater. Sci. Eng. C 104 (2019) 109890.

[41] F. Zhang, X. You, H. Dou, Z. Liu, B. Zuo, X. Zhang, Facile fabrication of robust silk nanofibril films via direct dissolution of silk in CaCl2–formic acid solution, ACS Appl. Mater. Interfaces 7 (5) (2015) 3352–3361.

[42] K. DeFrates, T. Markiewicz, K. Callaway, Y. Xue, J. Stanton, D. Salas-de la Cruz, X. Hu, Structure—property relationships of Thai silk—microcrystalline cellulose biocomposite materials fabricated from ionic liquid, Int. J. Biol. Macromol. 104 (2017) 919—928.

[43] X. Hu, K. Shmelev, L. Sun, E.-S. Gil, S.-H. Park, P. Cebe, D.L. Kaplan, Regulation of silk material structure by temperature-controlled water vapor annealing, Biomacromolecules 12 (5) (2011) 1686—1696.

[44] X. Hu, D. Kaplan, P. Cebe, Dynamic protein— water relationships during β-sheet formation, Macromolecules 41 (11) (2008) 3939—3948.

[45] J. Wang, Y. Cheng, L. Chen, T. Zhu, K. Ye, C. Jia, H. Wang, M. Zhu, C. Fan, X. Mo, In vitro and in vivo studies of electroactive reduced graphene oxide-modified nanofiber scaffolds for peripheral nerve regeneration, Acta Biomater. 84 (2019) 98—113.

[46] S. Ahn, C.O. Chantre, A.R. Gannon, J.U. Lind, P.H. Campbell, T. Grevesse, B.B. O'Connor, K.K. Parker, Soy protein/cellulose nanofiber scaffolds mimicking skin extracellular matrix for enhanced wound healing, Advanced healthcare materials 7 (9) (2018) 1701175.

[47] G. Perumal, P.M. Sivakumar, A.M. Nandkumar, M. Doble, Synthesis of magnesium phosphate nanoflakes and its PCL composite electrospun nanofiber scaffolds for bone tissue regeneration, Mater. Sci. Eng. C 109 (2020) 110527.

[48] S.H. Ku, S.H. Lee, C.B. Park, Synergic effects of nanofiber alignment and electroactivity on myoblast differentiation, Biomaterials 33 (26) (2012) 6098—6104.

[49] L. Wang, Y. Wu, T. Hu, P.X. Ma, B. Guo, Aligned conductive core-shell biomimetic scaffolds based on nanofiber yarns/hydrogel for enhanced 3D neurite outgrowth alignment and elongation, Acta Biomater. 96 (2019) 175—187.

[50] Y. Wu, L. Wang, B. Guo, P.X. Ma, Interwoven aligned conductive nanofiber yarn/hydrogel composite scaffolds for engineered 3D cardiac anisotropy, ACS Nano 11 (6) (2017) 5646—5659.

[51] P.K. Chakraborty, J. Adhikari, P. Saha, Facile fabrication of electrospun regenerated cellulose nanofiber scaffold for potential bone-tissue engineering application, Int. J. Biol. Macromol. 122 (2019) 644—652.

[52] D.A. Brennan, D. Jao, M.C. Siracusa, A.R. Wilkinson, X. Hu, V.Z. Beachley, Concurrent collection and post-drawing of individual electrospun polymer nanofibers to enhance macromolecular alignment and mechanical properties, Polymer 103 (2016) 243—250.

[53] X. Zhang, M.R. Reagan, D.L. Kaplan, Electrospun silk biomaterial scaffolds for regenerative medicine, Adv. Drug Deliv. Rev. 61 (12) (2009) 988—1006.

[54] A.A. Conte, K. Shirvani, H. Hones, A. Wildgoose, Y. Xue, R. Najjar, X. Hu, W. Xue, V.Z. Beachley, Effects of post-draw processing on the structure and functional properties of electrospun PVDF-HFP nanofibers, Polymer 171 (2019) 192—200.

[55] V. Beachley, X. Wen, Effect of electrospinning parameters on the nanofiber diameter and length, Mater. Sci. Eng. C 29 (3) (2009) 663—668.

[56] X. Hu, D. Kaplan, P. Cebe, Determining beta-sheet crystallinity in fibrous proteins by thermal analysis and infrared spectroscopy, Macromolecules 39 (18) (2006) 6161—6170.

[57] L. Wei, D. Zhou, X. Kang, Electrospinning as a novel strategy for the encapsulation of living probiotics in polyvinyl alcohol/silk fibroin, Innovat. Food Sci. Emerg. Technol. (2021) 102726.

[58] N. Forouzideh, S. Nadri, A. Fattahi, E.D. Abdolahinia, M. Habibizadeh, K. Rostamizadeh, A. Baradaran-Rafii, H. Bakhshandeh, Epigallocatechin gallate loaded electrospun silk fibroin scaffold with anti-angiogenic properties for corneal tissue engineering, J. Drug Deliv. Sci. Technol. 56 (2020) 101498.

[59] H.B. Wang, M.E. Mullins, J.M. Cregg, C.W. McCarthy, R.J. Gilbert, Varying the diameter of aligned electrospun fibers alters neurite outgrowth and Schwann cell migration, Acta Biomater. 6 (8) (2010) 2970—2978.

[60] Y. Liang, D. Wu, R. Fu, Carbon microfibers with hierarchical porous structure from electrospun fiber-like natural biopolymer, Sci. Rep. 3 (2013) 1119.

[61] F. Croisier, A.-S. Duwez, C. Jérôme, A. Léonard, K. Van Der Werf, P.J. Dijkstra, M.L. Bennink, Mechanical testing of electrospun PCL fibers, Acta Biomater. 8 (1) (2012) 218—224.

[62] X. Chen, Z. Shao, D.P. Knight, F. Vollrath, Conformation transition kinetics of Bombyx mori silk protein, Proteins: Structure, Function, and Bioinformatics 68 (1) (2007) 223—231.

[63] S. Ling, Z. Qi, D.P. Knight, Z. Shao, X. Chen, Synchrotron FTIR microspectroscopy of single natural silk fibers, Biomacromolecules 12 (9) (2011) 3344—3349.

[64] X. Hu, Q. Lu, L. Sun, P. Cebe, X. Wang, X. Zhang, D.L. Kaplan, Biomaterials from ultrasonication-induced silk fibroin— hyaluronic acid hydrogels, Biomacromolecules 11 (11) (2010) 3178—3188.

[65] P. Hernandez-Gomez, J. Munoz, C. Torres, C. de Francisco, O. Alejos, Influence of stoichiometry on the magnetic disaccommodation in barium M-type hexaferrites, J. Phys. Appl. Phys. 36 (9) (2003) 1062.

[66] I. Troyanchuk, S. Trukhanov, H. Szymczak, K. Baerner, Effect of oxygen content on the magnetic and transport properties of Pr0. 5Ba0. 5MnO3-γ, J. Phys. Condens. Matter 12 (7) (2000) L155.

[67] A. Kozlovskiy, K. Egizbek, M.V. Zdorovets, M. Ibragimova, A. Shumskaya, A.A. Rogachev, Z.V. Ignatovich, K. Kadyrzhanov, Evaluation of the efficiency of detection and capture of manganese in aqueous solutions of FeCeOx nanocomposites doped with Nb2O5, Sensors 20 (17) (2020) 4851.

[68] S. Trukhanov, D. Kozlenko, A. Trukhanov, High hydrostatic pressure effect on magnetic state of anion-deficient La0. 70Sr0. 30MnOx perovskite manganites, J. Magn. Magn Mater. 320 (14) (2008) e88—e91.

[69] S. Trukhanov, A. Trukhanov, H. Szymczak, Effect of magnetic fields on magnetic phase separation in anion-deficient manganite La0. 70Sr0. 30MnO2. 85, Low Temp. Phys. 37 (6) (2011) 465—469.

[70] Z. Xu, L. Shi, M. Yang, L. Zhu, Preparation and biomedical applications of silk fibroin-nanoparticles composites with enhanced properties-A review, Mater. Sci. Eng. C 95 (2019) 302—311.

[71] K. Zheng, J. Yu, W. Zhang, X. Li, Y. Fan, D.L. Kaplan, Self-assembling oxidized silk fibroin nanofibrils with controllable fractal dimensions, J. Mater. Chem. B 6 (28) (2018) 4656—4664.

[72] B.D. Lawrence, F. Omenetto, K. Chui, D.L. Kaplan, Processing methods to control silk fibroin film biomaterial features, J. Mater. Sci. 43 (21) (2008) 6967—6985.

[73] Y. Wang, R. Ma, K. Hu, S. Kim, G. Fang, Z. Shao, V.V. Tsukruk, Dramatic enhancement of graphene oxide/silk nanocomposite membranes: increasing toughness, strength, and Young's modulus via annealing of interfacial structures, ACS Appl. Mater. Interfaces 8 (37) (2016) 24962—24973.

[74] R. Pattanayak, S.P. Ghosh, S. Panigrahi, Effect of grain size on exchange-spring mechanism of [BaFe12O19 (BaM)-Na0. 5Bi0. 5TiO3 (NBT)] magnetoelectric composite system, J. Magn. Magn Mater. 482 (2019) 14—19.

[75] S. Trukhanov, V. Fedotova, A. Trukhanov, S. Stepin, H. Szymczak, Synthesis and structure of nanocrystalline La 0.50 Ba 0.50 MnO 3, Crystallogr. Rep. 53 (7) (2008) 1177—1180.

[76] D. Shlimas, A. Kozlovskiy, M. Zdorovets, Study of the formation effect of the cubic phase of LiTiO 2 on the structural, optical, and mechanical properties of Li 2±x Ti 1±x O 3 ceramics with different contents of the X component, J. Mater. Sci. Mater. Electron. 32 (6) (2021) 7410—7422.

[77] J. Wang, F. Zhao, W. Wu, G.-m. Zhao, Finite-size scaling relation of the Curie temperature in barium hexaferrite platelets, J. Appl. Phys. 110 (12) (2011) 123909.